Available online at www.sciencedirect.com

ScienceDirect

Geochimica et Cosmochimica Acta 282 (2020) 340–356

Geochimica et Cosmochimica Acta

www.elsevier.com/locate/gca

Metal isotope signatures from lava-seawater interaction during the 2018 eruption of Kīlauea

Nicholas J. Hawco [a,*,1], Shun-Chung Yang [a], Rhea K. Foreman [b], Carolina P. Funkey [b], Mathilde Dugenne [b], Angelicque E. White [b], Samuel T. Wilson [b], Rachel L. Kelly [a], Xiaopeng Bian [a], Kuo-Fang Huang [c], David M. Karl [b], Seth G. John [a]

[a] *Department of Earth Sciences, University of Southern California, Los Angeles, CA, United States*
[b] *Department of Oceanography, School of Ocean and Earth Sciences and Technology, University of Hawai'i at Mānoa, Honolulu, HI, United States*
[c] *Institute of Earth Sciences, Academia Sinica, Taipei, Taiwan*

Received 3 January 2020; accepted in revised form 4 May 2020; Available online 28 May 2020

Abstract

The 2018 eruption of Kīlauea was associated with massive input of molten lava into the coastal ocean, which altered seawater chemistry and increased phytoplankton production. In seawater plumes advected away from the site of lava entry, we observed elevated concentrations of over a dozen metals relative to background seawater and unique isotopic compositions of Fe, Cu, Ni, Cd and Zn. The δ^{56}Fe of iron released from lava was lower than basaltic, riverine and coastal iron from Hawai'i, but similar to observations of other high-temperature hydrothermal vent fluids. However, rapid precipitation led to only modest enrichments in dissolved iron (<10 nM), with increasing dissolved δ^{56}Fe likely due to fractionation associated with ligand-mediated dissolution of particulate Fe. The isotopic composition of copper and nickel show evidence for two-endmember mixing between background seawater and a lava source. While the Ni isotopic endmember reflected basaltic δ^{60}Ni, endmember δ^{65}Cu, δ^{66}Zn, and δ^{114}Cd were isotopically lighter than basalt. We hypothesize that high diffusivity and volatility of chalcophile elements leads to strong kinetic fractionation in rapidly cooling lavas, similar to Cu, Zn and Cd isotopic patterns observed in tektites. The isotopic signatures of Cu and Ni observed during the 2018 eruption of Kīlauea far exceed their normal seawater range and may be useful for identifying large-scale lava input into ocean waters during the formation of large igneous provinces and other episodes of volcanism.
© 2020 The Authors. Published by Elsevier Ltd. This is an open access article under the CC BY license (http://creativecommons.org/licenses/by/4.0/).

Keywords: Isotope fractionation; Forsterite; Iron; Nickel; Copper; Basalt; Hawaii

1. INTRODUCTION

Prior to 2018, Kīlauea on the island of Hawai'i had been erupting continuously since 1983, mainly from the Pu'u 'Ō'ō vent on the East Rift Zone of the volcano. Renewed eruption in 2018 led to the collapse of the Pu'u 'Ō'ō vent (30 April), the opening of new fissures further east (4

* Corresponding author.
E-mail address: hawco@hawaii.edu (N.J. Hawco).
[1] Present address: Department of Oceanography, School of Ocean and Earth Sciences and Technology, University of Hawai'i at Mānoa, Honolulu, HI, United States.

https://doi.org/10.1016/j.gca.2020.05.005
0016-7037/© 2020 The Authors. Published by Elsevier Ltd.
This is an open access article under the CC BY license (http://creativecommons.org/licenses/by/4.0/).

May), and a 20-fold greater lava effusion rate compared to average flow rates over the last 30 years (Neal et al., 2019). Lava from this eruption first reached the ocean along the island's southeastern coast on 23 May, intensifying as Fissure 8 became the main source of lava (27 May). By 5 June, channelized flow of fresh, less viscous lavas from Fissure 8 filled Kapoho Bay and continued to pour into the Pacific Ocean, creating large steam clouds from the boiling of seawater and 3.5 km^2 of new land mass (Neal et al., 2019). Lava entry to the ocean continued until 4 August, when eruption activity weakened substantially.

Coincident with the timing and location of lava entry to the ocean, a large increase in satellite-derived chlorophyll *a* concentration indicated that phytoplankton communities were stimulated by lava input (Fig. 1; Wilson et al., 2019). To validate these satellite measurements and understand the drivers of the apparent phytoplankton bloom, an expedition was mounted between 13–17 July, 2018 to sample ocean waters near the lava entry site. *In situ* measurements of chlorophyll *a* exceeded 0.6 μg L^{-1} and coincided with geochemical markers of lava-seawater interaction, such as high concentrations of silicate and metals (Sedwick et al., 1991; Resing and Sansone, 2002; Wilson et al., 2019). Elevated concentrations of nitrate were also measured in the plume, which promoted the rapid growth of diatoms in waters that are typically limited by nitrogen scarcity. The isotopic composition of nitrate was consistent with a deep water source, suggesting that the flow of molten lava down the island slope resulted in heating of cold mesopelagic waters rich in nitrate, which ascended to the ocean surface, fueling biological production (Wilson et al., 2019).

Although lava production from the 2018 eruption was large (~0.8 km^3) in comparison to mean lava production rates at Kīlauea over the last several decades (0.11 km^3 $year^{-1}$), it is dwarfed by past eruptions associated with the emplacement of large igneous provinces, which have volumes of hundreds of thousands to millions of km^3 (Coffin and Eldholm, 1993; Bryan et al., 2010; Neal et al., 2019). A number of these eruptions (but not all) are associated with major mass extinctions (Wignall, 2001; Bryan et al., 2010). Trigger mechanisms associated with these events have focused on perturbations to the carbon cycle: outgassing of volcanic CO_2 leading to global warming, ocean stratification, and anoxia, as well as ocean acidification. However, the 2018 eruption of Kīlauea indicates that more direct perturbations associated with ocean circulation

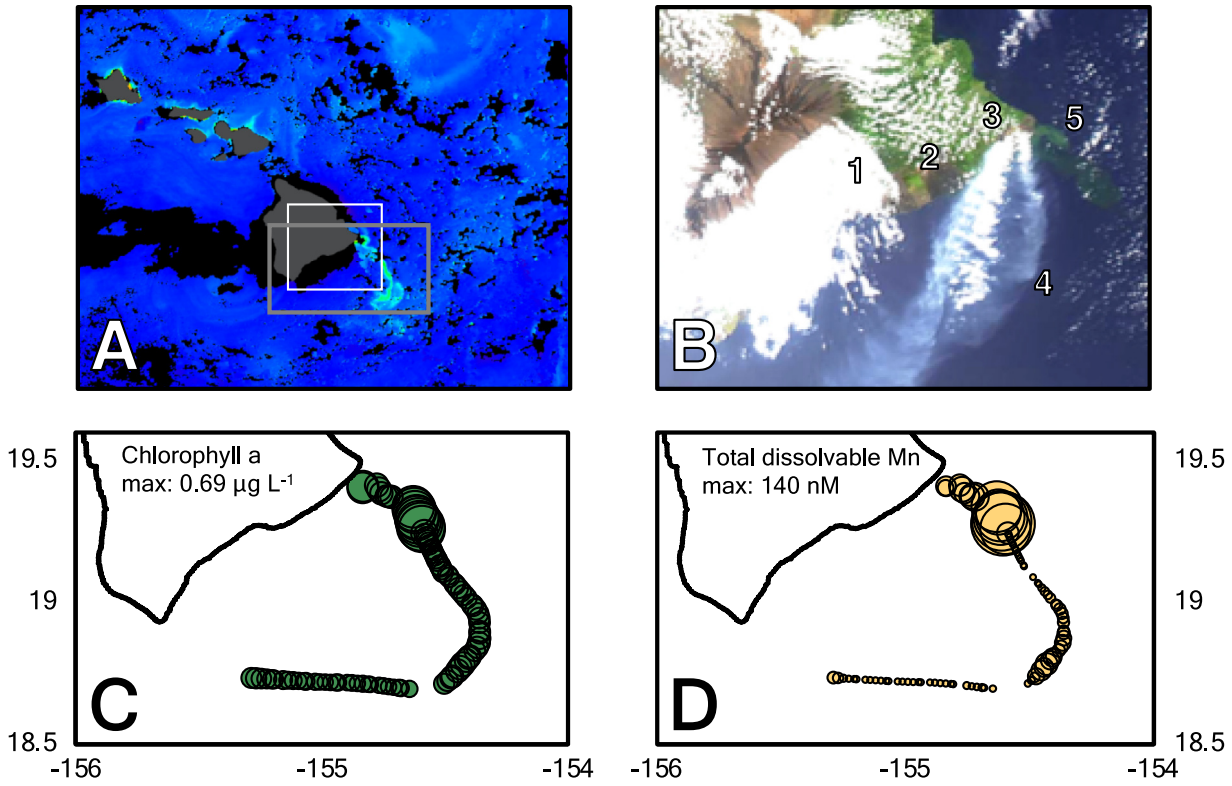

Fig. 1. (A) Satellite chlorophyll *a* observations from July 10, 2018, three days before the sampling expedition. Elevated chlorophyll *a* concentrations stemming from the eastern point of the Island of Hawai'i can be seen. The southeast-ward spread of this plume tracks the flow of surface waters (Wilson et al., 2019). The white rectangle describes the region plotted in B; the grey rectangle describes the region plotted in C and D. (B) Satellite image of the Island of Hawai'i on June 18, 2018. Numbers highlight approximate locations of Kīlauea summit (1), Pu'u 'Ō'ō vent (2), and Fissure 8 (3). Visible signatures of lava-seawater interaction include steam clouds (4) and surface ocean discoloration (5). Note that this image has been brightened to improve visibility. Data were assembled using NASA Worldview from 1 km daily chlorophyll *a* retrievals (Panel A) and corrected reflectance (Panel B), both from the MODIS Aqua satellite (https://worldview.earthdata.nasa.gov/). (C) *In situ* measurements of chlorophyll *a* collected from the ship's underway system while the tow-fish was deployed. Chlorophyll *a* concentration is proportional to circle area (max. 0.69 μg L^{-1} and min. 0.07 μg L^{-1}). (D) Total dissolvable Mn concentrations from tow-fish samples (max: 140 nM; min: 1.1 nM). Plumes were encountered at 19.26°N (major) and 18.77°N (minor).

and nutrient supply are possible. It is unclear what effect these processes may have had during large volcanic eruptions in the past, in part because it is difficult to distinguish direct lava-seawater interaction from the subsequent weathering of basaltic rock on land.

Here, we investigate the elemental and isotopic signature of lava input into the North Pacific Ocean during the 2018 eruption of Kīlauea. Unique, light isotope composition in seawater Cu, Cd, and Zn suggest that these elements, especially Cu, may be useful for reconstructing episodes of direct lava-seawater interaction in the past oceans.

2. METHODS

2.1. Sampling

Sampling was conducted during the Hawai'i Ocean Time-series: Life Aquatic in the Volcanic Aftermath (HOT-LAVA; KOK1806) expedition on the R/V Ka'imikai-O-Kanaloa between July 13–18, 2018. All samples were collected from the ocean surface (depth range 1–3 m) using an underway tow-fish, deployed midship off the starboard side via a telescoping boom, and sampled at a ship speed of 4–7 kn. Semi-transparent polyethylene tubing (1/2″ OD) connected the sample inlet to an all-polytetrafluoroethylene (PTFE) bellows pump (St. Gobain, model PFD2) operating on deck via the ship's compressed air source at 50 psi. Additional tubing led pumped seawater into a HEPA-filtered, trace metal-free bubble within a laboratory van. Based on the approximate length of tubing between the tow-fish inlet and our sampling location (~60 m, roughly 8 L volume), and the flow rate (~1 L min^{-1}), the residence time of water in the tubing was roughly 8 minutes. Inside the van, T-junctures split two sampling lines from the main flow. One sample line was connected to an Acropak 1500 cartridge filter (0.2 μm, Pall) and used for collection of filtered samples while the second sample line was used to collect unfiltered samples.

Samples were collected at approximately 10 min intervals (roughly 1.5 km apart at a ship speed of 5 kn). Metal-free 50 mL centrifuge tubes (VWR) were rinsed and filled with either filtered or unfiltered seawater. Isotope samples were collected hourly from the filtered seawater line in 1 or 2 L polyethylene bottles. Prior to the cruise, bottles, centrifuge tubes, and sampling lines were soaked overnight in a 2% Citranox solution (Alconox), rinsed with 18.2 MΩ-cm water, soaked for 1 week in 10% hydrochloric acid (HCl), and rinsed several times again in 18.2 MΩ-cm water. Six unfiltered samples were also collected from the Wailuku River and coastal waters on the island of Hawai'i immediately prior to our expedition.

Chlorophyll *a* fluorescence was measured by an ECO-triplet fluorometer (SeaBird) from the ship's underway seawater supply. Underway images were collected using an Imaging FlowCytoBot (McLane Research Laboratories), also connected to the ships underway line. Image collection was triggered by both scattering and fluorescence thresholds. Data from this expedition can be accessed at http://ifcb-data.soest.hawaii.edu/HOTLAVA.

2.2. Metal concentration analyses

Following the expedition, dissolved and total dissolvable metal samples (filtered and unfiltered samples, respectively) were acidified to pH = 1.8 with concentrated, distilled HCl (0.1% v/v), and left for > 1 month. Samples were aliquoted into 15 mL acid-washed centrifuge tubes and amended with 50 μL of an isotope spike containing ^{57}Fe, ^{62}Ni, ^{65}Cu, ^{67}Zn, and ^{110}Cd. Metals were extracted with Nobias PA-1 resin with a SeaFAST preconcentration system (Elemental Scientific) and eluted into 3 M nitric acid containing 1 ppb In. Extracted metals were analyzed by inductively coupled plasma mass spectrometry (ICP-MS) on an Element 2 Instrument (Thermo). Mo, Sn, Pd, Cd, Ce, La, Nd, Pr, Sm and Eu were measured in low resolution mode whereas Mn, Fe, Co, Ni, Cu, and Zn were analyzed in medium resolution. Concentrations of Fe, Ni, Cu, Zn and Cd were derived via isotope dilution, with daily calibration of the added isotope spike against a consistent 10 ppb natural abundance solution diluted from a certified reference (Inorganic Ventures). For Cd, a correction for MoO^+ interference on ^{110}Cd and ^{114}Cd was applied based on signal intensity of ^{95}Mo and a run-specific instrument response determined with an analysis of an in-house seawater sample with and without addition of ~50 μM Mo, also processed through the SeaFAST. Cadmium intensity was further corrected for isobaric interferences by Pd and Sn by monitoring ^{105}Pd and ^{118}Sn.

Following ^{115}In correction for sample matrix effects, concentrations of Mn, Co and rare earth elements (REE) were quantified relative to the 10 ppb standard and corrected for incomplete sample loading by the recovery of the ^{62}Ni spike, which was typically 50–80% (Fig. S1). This procedure was also used to quantify Cu and Fe at peak concentrations, where measured isotope ratios were similar to natural abundances and values derived from isotope dilution were not reliable. Dilutions of these high metal samples were used to confirm that this approach was appropriate (see Electronic Annex). Prior analyses of the GEOTRACES community reference standard GSP yielded concentrations of 0.18 nM Fe, 0.04 nM Zn, 2.53 nM Ni, 0.58 nM Cu, and 0.79 nM Mn, which agrees with consensus values for these elements (see Table S1). Consensus values for REEs are not available for this standard, but REE concentrations in non-plume waters compare well with published measurements in the North Pacific surface waters (Table S1; Fröllje et al., 2016).

Preconcentration blanks were determined by processing 10 mM HCl amended with isotope spike solution. Median blanks (n = 25) were subtracted from all samples (Table S1). Although blanks processed immediately after high concentration samples (e.g. 1 μM total dissolvable Fe) were several-fold greater than typical blanks, the magnitude of the carryover effect was small, (<1% of the previous sample, Figs. S2 and S3) and no attempt was made to correct for sample carryover (see Electronic Annex).

As samples were not UV-oxidized, cobalt concentrations reflect a labile quantity available for ligand extraction following acidication to pH = 1.8 (Biller and Bruland, 2012) that underestimates actual dissolved cobalt concentrations

in background waters. Acidification may release some amount of cobalt from strong ligands at seawater pH; as a result, this quantity is not necessarily equal to 'labile cobalt' measurements from electrochemical measurements at pH ~ 8. The lack of UV oxidation may also lead to an underestimate of dissolved Cu concentration (Biller and Bruland, 2012; Posacka et al., 2017). At present, however, it remains unclear whether added ^{65}Cu can equilibrate with the entire spectrum of Cu ligand complexes in seawater. Isotope dilution methods quantifying the SAFE S standard (collected at the same location as GSP) did not find significantly different Cu concentrations in UV-oxidized samples, but UV oxidation led to a ~ 10% increase in dCu in deeper waters (Milne et al., 2010).

2.3. Purification of Fe, Zn, and Cd for isotopic analysis

To determine the isotopic composition of Cd, Cu, Ni, Fe, and Zn, metals were extracted from 1L or 2L samples and purified by anion exchange chromatography (Conway et al., 2013). Prior to extraction, 1L bottles were amended with double isotope spikes of ^{57}Fe and ^{58}Fe, ^{64}Zn and ^{67}Zn, and ^{110}Cd and ^{112}Cd in a spike-to-sample ratio of 2:1 for Fe, and 1:1 for Zn and Cd. Metals were extracted from seawater using a two-step protocol. Nobias PA-1 resin was added to pH = 1.8 seawater and shaken overnight on a shaker table. The pH of the solution was then increased to 6.0 ± 0.2 by addition of an ammonium acetate buffer (final concentration ~15 mM) and shaken for ~5 hr. Afterward, the resin was filtered from the solution by pouring through an acid-washed, 8 μm polycarbonate filter (Whatman), rinsed thoroughly with 18.2 MΩ-cm water and eluted in 3 M HNO_3. The sample was evaporated to dryness on a hot plate overnight, digested with 1:1 HCl:HNO_3 for > 2 hours, and evaporated to dryness again. Extracted metals were subsequently dissolved in 10 M HCl.

Metals were purified for isotopic analysis via anion exchange chromatography with AG-MP1 resin in microcolumns as described by Conway et al. (2013). A multistep purification method for Cu and Ni was developed to complement previously implemented protocols for separation of Fe, Zn and Cd (Fig. S4). Separation of Cu was achieved by AG-MP1 resin while Ni required additional purification by Nobias PA-1 resin, followed by another separation using AG-MP1 to remove contaminants. A full description and evaluation of this method is presented by Yang et al. (2020), and the protocol is outlined in the Electronic Annex.

2.4. Isotopic measurements, accuracy and reproducibility

The isotopic composition of Fe, Ni, Cu, Zn and Cd (δ^{56}Fe, δ^{65}Cu, δ^{60}Ni, δ^{66}Zn, and δ^{114}Cd) were measured on a Neptune Plus MC-ICPMS (Thermo Scientific) at the institute of Earth Sciences, Academia Sinica, Taiwan. Analysis details are described in the Electronic Annex. The precision for the reported isotopic composition of each sample was obtained by combining the standard error (2SE) of both sample and standard measurements (Conway et al., 2013). The accuracy of our analytical conditions was verified by determining the isotopic composition of secondary isotope standards for each element on the same analysis day (Table 1). These values are consistent with reported values previously.

To avoid potential isotopic fractionation by chromatographic separation, Ni and Cu recovery must be ~100% during anion exchange chromatography. On average, 84 ± 4% of Cu and 96 ± 3% Ni were recovered from column chemistry for this sample set. Recovery experiments indicated that >99% of both Cu and Ni is recovered during ion exchange chromatography (Yang et al., 2020), implying that incomplete sample recovery occurs during extraction of these metals from seawater, not during the subsequent column chemistry. Low recovery of Cu may result from strong ligands in seawater that do not allow for 100% extraction of Cu but are isotopically equilibrated during concentration measurements by isotope dilution. Using the same protocols, a similar recovery (86 ± 3% for Cu, 102 ± 3% for Ni) was also found for a dataset collected in the North Pacific Ocean, which found a more narrow range of isotopic variation (δ^{65}Cu = +0.62 ± 0.10 ‰, 1SD, n = 48; δ^{60}Ni = +1.51 ± 0.11 ‰, 1SD, n = 45) than the 1–2 ‰ variation found in this dataset (Table 2). These values, as well as seawater measurements of δ^{65}Cu and δ^{60}Ni outside of plume waters are consistent with other published datasets for the North Pacific, South Pacific, and elsewhere (Yang et al., 2020). Thus, although non-quantitative recovery can introduce bias into measurements, there is little evidence that it is responsible for the isotopic variations reported here.

3. RESULTS

In the timeline of the 2018 eruption, the HOT-LAVA expedition occurred roughly 1 month after Kapoho Bay was filled, while lava originating primarily from Fissure 8 was entering the ocean at an estimated rate of 50–100 m^3 s^{-1} (Neal et al., 2019). During the expedition, surface currents flowed southeastward, following the rim of a cyclonic eddy located northeast of the Island of Hawai'i (Wilson et al., 2019). Sampling patterns were guided by satellite-based chlorophyll *a* images obtained prior to the expedition, which showed filaments of high chlorophyll *a* waters originating from the site of lava entry at Kapoho (Fig. 1A; Wilson et al., 2019). Surface waters in the immediate vicinity of lava entry bore a rich brown color and a large cloud of steam from the mixture of lava and ocean water was visible (Fig. 1B), but safety concerns prevented sampling within 1 km of the lava entry site. At this distance, thermal anomalies were not detected, even in waters that were visibly discolored. Although the change in ocean color was affected by an abundance of inorganic particles, elevated chlorophyll *a* observed by satellite was validated by measurements of underway chlorophyll *a* (Fig. 1C) and high rates of primary production (Wilson et al., 2019).

Advection of chlorophyll-rich waters away from the lava entry site generally followed a southeast-ward direction, but varied daily due to the influence of the passing eddy. Poor satellite coverage during the expedition led to collection of a number of samples in un-impacted surface seawater with

Table 1
Evaluation of secondary isotopic standards.

	Secondary standard	Value ± 2SD (‰)	n	Literature Value (‰)
δ^{56}Fe	NIST SRM 3126a	0.33 ± 0.08	18	+0.35 ± 0.01 (35) [1]
δ^{60}Ni	Wako-Ni	−0.29 ± 0.08	21	−0.28 ± 0.03 (16) [2]
δ^{63}Cu	Wako-Cu	0.27 ± 0.07	65	+0.28 ± 0.03 (19) [2]
δ^{66}Zn	AA-ETH	0.29 ± 0.04	13	+0.28 ± 0.02 (110) [3]
δ^{114}Cd	BAM1012	−1.34 ± 0.24	11	−1.33 ± 0.04 (138) [4]

[1] Stevenson et al. (2017).
[2] Takano et al. (2017).
[3] Archer et al. (2017).
[4] Abouchami et al. (2013).

low metal concentrations. When plumes of lava-impacted seawater were crossed (originally identified by chlorophyll *a* fluorescence > 0.2 μg L^{-1}), concentrations of all total dissolvable metals increased in unison (Fig. 2). The peak of this plume occurred at 19.28°N and 154.61°W (Fig. 1D). For Mn, Ni, and labile Co, peak total dissolvable metal concentrations (140, 10.3, and 2.7 nM, respectively) were similar to dissolved metal concentrations collected at the same time (146, 9.9, and 2.7 nM; Figs. 3 and 4A,B). For Fe, Ce, and Nd, total dissolvable concentrations (1450 nM, 103 pM, and 87 pM, respectively) exceeded dissolved concentrations (6 nM, 11 pM, 8 pM) due to the presence of a large particulate pool of these metals (Fig. 4D-F). Other elements (e.g. Cu), represented an intermediate case (Fig. 4C). Following the first plume, the dissolved concentration of some of these metals (especially Fe, Cu and Ce) did not return to background concentrations as quickly as total dissolvable concentrations, suggesting redissolution of particulate metals caught in the cartridge filter (Fig. S5). This effect was negligible for metals that did not have a significant particulate concentration (Mn, Ni, and Co).

A second region of high metal concentration was encountered at 18.78°N, 154.43°W, where chlorophyll *a* was slightly elevated (0.15 μg L^{-1}) compared to background waters (0.07–0.12 μg L^{-1}; Fig. 1D). Elemental patterns in this second, minor plume were similar to that encountered in the first plume (Fig. 5). Both features likely originated from the same location, differing primarily in age and extent of mixing with background seawater.

The isotopic composition of Fe, Ni, Cu, Zn and Cd were determined within plume waters. Total dissolvable iron (tdFe) samples from lava impacted seawater ranged from −0.62‰ to −0.47‰ (Fig. 6), while riverine and coastal samples far from the plume contained a δ^{56}Fe between −0.18‰ and 0‰. Close to the site of lava entry, dissolved δ^{56}Fe in plume waters was also negative, but not as low as tdFe samples: between −0.13 and −0.41‰. Samples collected further offshore were isotopically heavier and ranged between +0.02 and +0.25‰. Some of these measurements are impacted by the redissolution of particulate Fe after the first plume was crossed (Table 2A); the implications of this latent "contamination" are discussed later. Large variations were also observed for the isotopic composition of dissolved Ni (+0.61‰ to +1.69‰) and dissolved Cu (−1.79‰ to +0.33‰), with lower values reflecting higher concentrations for both elements (Fig. 7). For Zn and Cd, concentrations were too low to generate reliable isotopic measurements, except for 3 samples in the center of the lava-seawater plume (Table 2A). In samples where dZn exceeded 1 nM, δ^{66}Zn varied between −0.10‰ to −0.03‰; in samples where dCd exceeded 20 pM, δ^{114}Cd varied between −0.66 and −0.18‰.

4. DISCUSSION

4.1. Elemental signatures in surface water plumes

Concentrations of metals sampled by underway tow-fish revealed a similar pattern to chlorophyll *a*, even in offshore waters far from the lava entry site (Fig. 2). This is best illustrated in the distribution of Mn, which has a long history of tracing hydrothermal input over great distances (Klinkhammer et al., 1977; Klinkhammer et al., 1985; Resing et al., 2015). Compared to dissolved Mn concentrations (dMn) of ~1.5 nM in background seawater, concentrations within the plume reached 140 nM and overlapped with the highest chlorophyll *a* concentrations (exceeding 0.6 μg L^{-1}; Fig. 2). A second, more dilute plume of lava-impacted water was encountered much farther offshore, where dMn reached 15 nM (Fig. 2). In both plumes, 0.2 μm filtered samples (dMn) yielded identical Mn concentrations as unfiltered samples (total dissolvable Mn or tdMn; slope = 1.06, R^2 = 0.99), implying insignificant scavenging of Mn on the timescale of plume advection and dilution (Fig. 3). Although relatively rapid scavenging of Mn has been observed in deep ocean hydrothermal vent plumes (Cowen et al., 1990), the stability of Mn in lava-impacted surface waters is consistent with photo-inhibition of biological Mn oxidation in the euphotic zone (Sunda and Huntsman, 1988). As a result, we interpret Mn distributions as an essentially conservative tracer of lava input during the 2018 eruption.

High concentrations of Mn in surface waters were mirrored in a number of other elements. There is a particularly strong correlation between Mn and labile Co (R^2 = 0.999), which also had equivalent concentrations in filtered and unfiltered samples (Fig. 4A). Co-precipitation during manganese oxide formation is also the main sink for Co in seawater (Moffett and Ho, 1996; Hawco et al., 2018), further

Table 2
Isotopic data for surface seawater and related samples during the 2018 eruption.

A. Dissolved metal samples (0.2 μm filtered)

Lat. °N	Lon. °W	dFe (nM)	δ^{56}Fe (±2SE, ‰)		dCu (nM)	δ^{63}Cu (±2SE, ‰)		dNi (nM)	δ^{60}Ni (±2SE, ‰)		dZn (nM)	δ^{66}Zn (±2SE, ‰)		dCd (pM)	δ^{114}Cd (±2SE, ‰)	
19.41	154.84	6.87	−0.26	0.09	32.26	−1.75	0.07	8.81	0.61	0.05	3.08	−0.10	0.06	48.8	−0.66	0.17
19.41	154.84	7.06	−0.34	0.07	5.58	−1.76	0.10	3.11	1.16	0.05	0.63			7.7		
19.42	154.78	7.18	−0.41	0.08	5.13	−1.48	0.09	2.92	1.19	0.06	0.51			6.0		
19.38	154.73	6.91	−0.32	0.08	6.80	−1.60	0.06	3.63			0.70			10.6		
19.34	154.63	7.31	−0.13	0.08	17.62	−1.79	0.07	6.97	0.74	0.06	2.07	−0.03	0.06	30.1	−0.18	0.17
19.28	154.61	6.69	−0.29	0.07	24.76	−1.66	0.05	9.73	0.83	0.06	3.25	−0.06	0.05	50.9	−0.48	0.15
19.22	154.58	3.30*	0.19	0.08	3.12*	−1.48	0.12	2.31	1.69	0.05	0.20			0.3		
19.17	154.54	3.10*	0.11	0.08	2.07*	−1.16	0.10	2.39	1.60	0.05	0.10			0.5		
19.11	154.51	2.57*	0.08	0.07	1.57*	−0.86	0.10	2.52	1.68	0.06	0.10			0.6		
19.10	154.49	3.38*	0.09	0.08	2.34*	−1.39	0.10	2.34	1.68	0.06	0.17			0.7		
19.04	154.44	3.64	0.04	0.08	2.57*	−1.39	0.11	2.54	1.59	0.06	0.13			1.4		
18.96	154.37	3.65	0.13	0.09	2.70	−1.47	0.09	2.61	1.56	0.06	0.13			2.4		
18.86	154.37	3.92	0.18	0.07	4.68	−1.79	0.11	2.97	1.32	0.07	0.25			5.7		
18.78	154.43	4.08	0.11	0.08	8.10	−1.84	0.09	3.38	1.16	0.06	0.48			9.5		
18.72	154.51	2.26	0.12	0.08	1.43*	−0.98	0.11	2.46	1.63	0.05	0.06			0.6		
18.70	154.69	2.98*	0.25	0.08	1.82*	−1.17	0.09	2.39	1.63	0.06	0.10			0.6		
18.71	154.82	2.22*	0.17	0.09	1.20*	−0.80	0.11	2.45	1.68	0.05	0.07			0.5		
18.72	154.95	2.43*	0.20	0.07	1.16*	−0.76	0.10	2.39	1.63	0.06	0.04			0.6		
18.72	155.08	1.05*	0.31	0.09	0.73	0.33	0.11	2.45	1.61	0.06	0.06			0.3		
18.73	155.21	0.61	0.02	0.13	0.63	0.28	0.14	2.41	1.62	0.06	0.06			0.5		

B. Total dissolvable metal samples (unfiltered)

Lat. °N	Lon. °W	tdFe (nM)	δ^{56}Fe (±2SE, ‰)		Note
19.42	154.78	254.6	−0.54	0.07	
19.39	154.76	207.9	−0.57	0.07	
19.38	154.73	325.3	−0.60	0.08	
19.34	154.63	1106	−0.56	0.10	
19.32	154.63	953.5	−0.59	0.09	
19.30	154.62	1386	−0.62	0.07	
19.28	154.61	2155	−0.51	0.08	
19.26	154.60	1216	−0.59	0.07	
18.78	154.43	117.3	−0.49	0.06	Minor plume
18.76	154.45	121.1	−0.47	0.07	Minor plume

C. Total dissolvable metal samples (unfiltered), Wailuku River and Coastal Hawai'i

Lat. °N	Lon. °W	tdFe (nM)	δ^{56}Fe (±2SE, ‰)		
19.72	155.14	2102	−0.06	0.08	Wailuku River, near LK falls
19.72	155.11	2702	−0.03	0.07	Wailuku River, near Rainbow falls
19.73	155.09	2181	0.00	0.08	Wailuku River Mouth, Hilo
19.72	155.06	37.2	−0.18	0.13	Hilo Bay, Hilo
20.02	155.82	253.2	−0.12	0.07	Spencer Beach Park
19.85	155.93	289.4	0.00	0.08	Queens Bath, Kiholo Bay

*Dissolved concentration > 30% greater than total dissolvable concentration, suggestive of particulate metal dissolution within filter.

implying that Mn oxidation was not active in surface waters. Strong correlations ($R^2 > 0.9$) were also observed between dMn and dissolved silicate, Ni, Cu, Zn, Cd, and between tdMn and total dissolvable Fe, La, Nd, Ce and several other rare earth elements, as well as total dissolvable Ni, Cu, Cd, and Zn (Figs. 2 and 4B-F). To a first order, the relative abundance of these elements is proportional to their abundance in Hawai'ian basalt (Govindaraju, 1994; Resing and Sansone, 2002), with the exception of Cu and Cd, which are enriched 3- and 16-fold, respectively, relative to the amount of Mn measured in the plume (Fig. 5A). There are also small deficits in silicate, Fe and rare earth elements, compared to their abundance in basalt, that likely reflect scavenging.

During a previous eruption at Kīlauea, Resing and Sansone (2002) conducted solubilization experiments with molten lava added to deionized water. Three major processes were identified from these experiments: (1) congruent dissolution whereby elements are added to seawater in proportion to their abundance in basaltic lava, (2) additional release of volatile elements during intensified degassing upon seawater lava mixing, and (3) reprecipitation of insol-

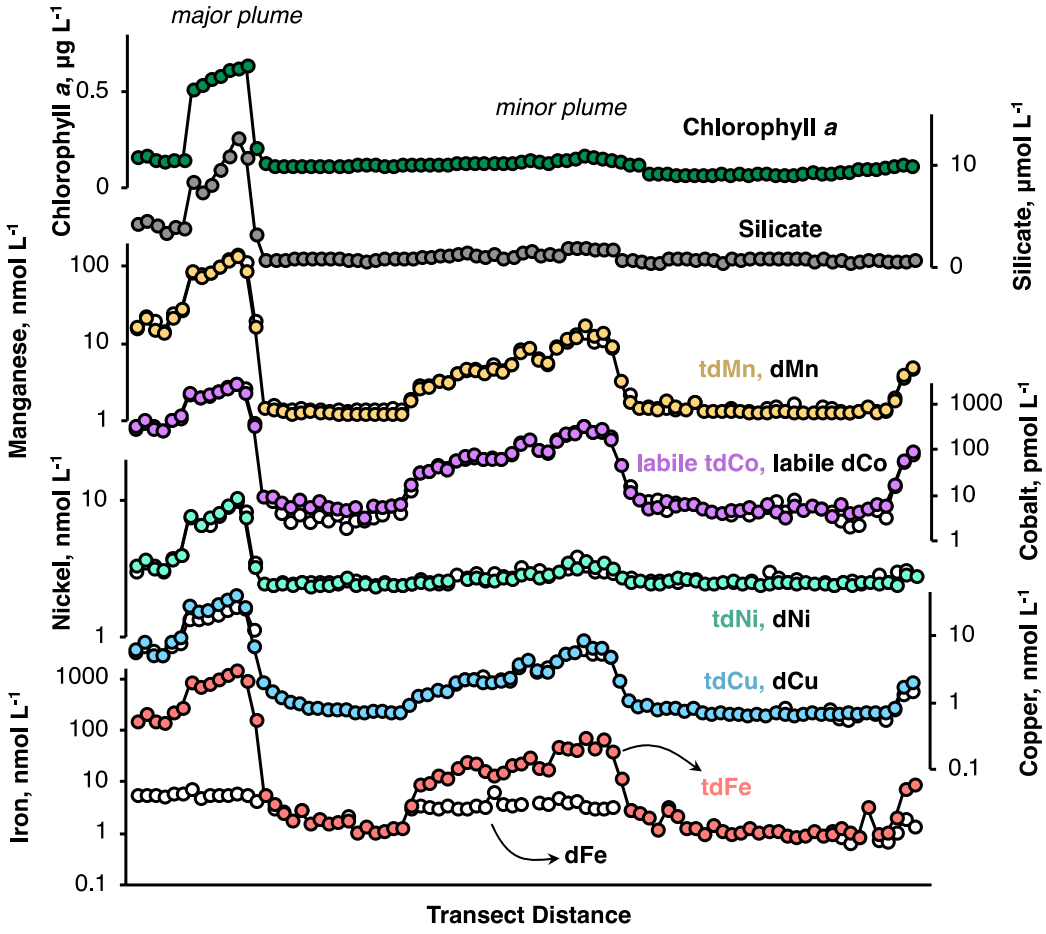

Fig. 2. Covariation in chlorophyll *a*, silicate, and metal abundance in a surface transect crossing lava-impacted plume waters, beginning near the site of lava entry (left) and heading further offshore (righthand side). For Mn, Co, Ni, Cu, and Fe, colored circles represent total dissolvable metal concentrations, which refer to unfiltered samples. Dissolved concentrations of Mn, Co, Ni, Cu and Fe are plotted in white circles on the same axes. Note that Mn, Co, Ni, Cu, and Fe are plotted on log scales. Sample locations are shown in Fig. 1C, D.

uble elements (Resing and Sansone, 2002). Normalized to Mn, the elemental pattern recovered from solubilization experiments is almost perfectly reproduced in the surface water plumes measured in 2018 (Fig. 5B), with power law regressions between these incubations and the primary and secondary surface plumes having correlation coefficients (R^2) of 0.99 and 0.98, respectively. However, Cd in surface waters was not as enriched as expected from solubilization experiments. Because Cd is highly volatile during high temperature magmatic processes (Rubin, 1997), it is possible that a significant fraction of lava-derived Cd was partitioned into vapor phases during lava-seawater mixture and exited to the atmosphere (Sansone et al., 2002).

It is intriguing that this level of chemical enrichment can occur without discernable changes in surface temperatures (26 °C). In the Resing and Sansone (2002) experiments, similar degrees of Mn release were associated with a temperature anomaly of roughly 15–20 °C. In 2018, much of the anticipated temperature increase was likely lost to thermocline waters as lava flowed down the island slope, which subsequently rose to the surface (Wilson et al., 2019). Based on the concentration and isotopic composition of nitrate observed in plume waters, this source water was likely from 300–500 m depth, bearing a potential temperature of 7–13 °C (Wilson et al., 2019). Any remaining temperature anomaly may have dissipated to the atmosphere shortly after reaching the surface. A number of metals are also enriched in subsurface waters and upwelling from 300–500 m depth can also represent a significant source. However, based on metal:NO_3 ratios associated with this depth range (Bruland, 1980; Conway and John, 2015) and peak NO_3 concentrations observed in tow-fish samples (0.9 µM), estimated upwelling concentrations of Ni, Cu, Fe, and Zn are far overshadowed by their release from lava (<3% from upwelling; Table S2). Due to its relatively low abundance in basalt, Cd remains an exception: upwelling of Cd can account for up to 26% of the concentration measured in plume waters. This may indicate an even greater loss of lava-derived Cd into the atmosphere.

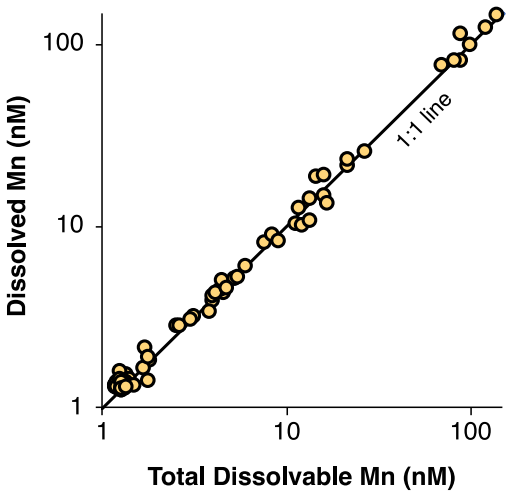

Fig. 3. Comparison between dissolved Mn from 0.2 μm filtered samples and total dissolvable Mn concentrations from unfiltered samples. Measurements are correlated ($R^2 = 0.99$) with a slope near a 1:1 line, indicating limited scavenging of manganese in lava-impacted plume waters.

4.2. Modification of iron isotope signatures during precipitation

In contrast to Mn, the reactivity of Fe following release from lava was immediate and intense. Total dissolvable Fe concentrations exceeded 1 μM in plume waters, but dissolved Fe concentrations plateaued at ~ 7 nM in the main plume, suggesting that > 99% of iron released from lava had precipitated (Fig. 4D). The ratio of tdFe to tdMn in the main plume was approximately 10:1, which is very similar to the ratio found in solubility experiments (7.5:1; Resing and Sansone, 2002). Given the negligible concentrations of particulate Mn, the strong partitioning of Fe into particulate phases suggests that the micromolar levels of particulate Fe do not represent fragments of intact basalt. If this were the case, tdMn would have exceeded dMn by 20 nM in the major plume, which was not observed (Fig. 3). Instead, Fe was originally dissolved and subsequently precipitated as an iron oxyhydroxide. Images collected by underway Imaging Flow CytoBot appear to show an abundance of amorphous mineral solids, sometimes entangled in organic detritus (Fig. 8). Most likely precipitated iron oxyhydroxides, these putative mineral-organic aggregates were also observed in the minor plume, where tdFe reached 71 nM but at a lower Fe:Mn ratio (4.3), suggesting some sinking of particulate iron during offshore transport.

The isotopic composition of iron (δ^{56}Fe) collected close to the lava entry site was light relative to basalt. Eight samples containing tdFe > 200 nM exhibited a very narrow of range of δ^{56}Fe, equal to -0.57 ± 0.04‰ (1SD; Fig. 6, Table 2). A similar δ^{56}Fe was observed in two samples from the secondary plume (-0.49 ± 0.06‰ and -0.47 ± 0.07‰, 2SE). The light isotopic composition is distinct from the δ^{56}Fe of mid-ocean ridge basalts and ocean island basalts

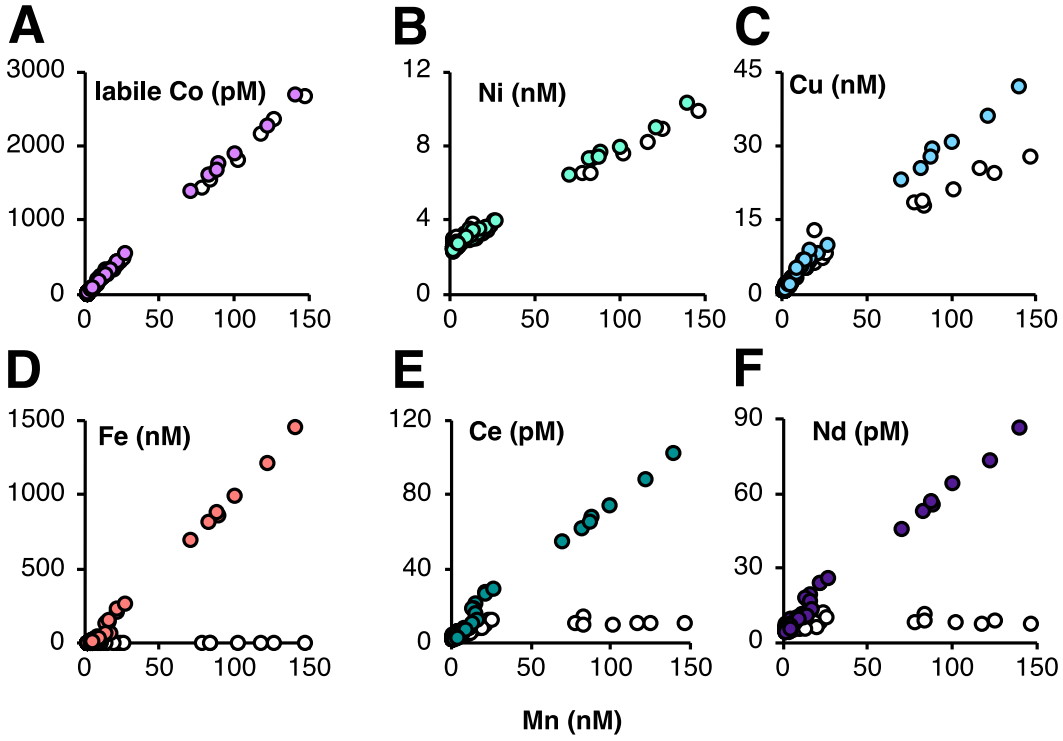

Fig. 4. Relationships between manganese concentrations in plume waters and labile Co (A), Ni (B), Cu (C), Fe (D), Ce (E), and Nd (F). In all cases, filled circles show total dissolvable metal concentrations, plotted against tdMn, while open circles show dissolved metal concentrations, plotted against dMn. Note the relatively consistent correlations for Co and Ni in both sample types, in contrast to dissolved Fe, Ce, and Nd.

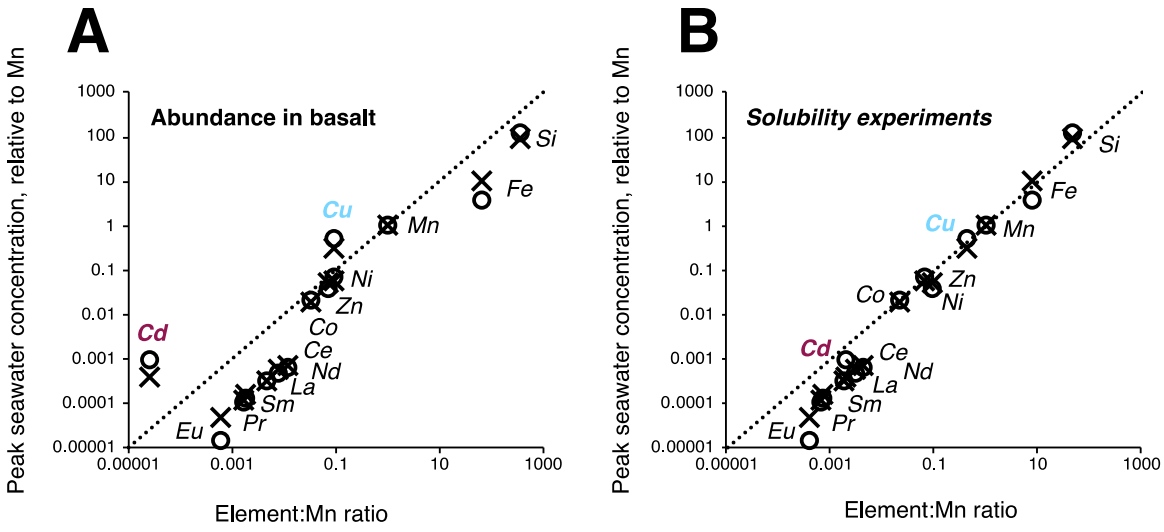

Fig. 5. Elemental signatures from the major (X) and minor (O) surface water plumes encountered during the 2018 eruption, compared to the composition of Hawai'ian basalt (A) or the elemental abundance released into deionized water during mixing experiments with lava from Kīlauea (B). All elements are normalized to Mn abundance and a dotted 1:1 line is shown for reference. Basalt composition and data from solubility experiments can be found in Resing and Sansone (2002).

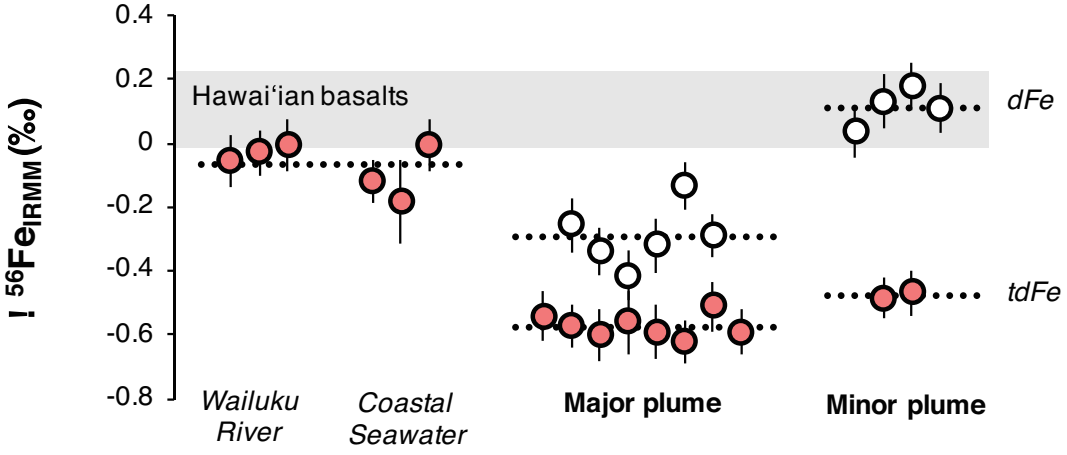

Fig. 6. Iron isotope composition (as $\delta^{56}Fe_{IRMM}$) of total dissolvable Fe (filled circles) and dissolved Fe (open circles). The $\delta^{56}Fe$ of Hawai'ian basalts is informed by Teng et al., 2008 and Teng et al., 2013. See Table 2 for additional information.

(Teng et al., 2013), which have a $\delta^{56}Fe$ between 0 and +0.2‰, including those from past eruptions at Kīlauea (Teng et al., 2008). We therefore infer that the bulk lava produced from the 2018 eruption also contained an Fe isotopic composition close to 0‰ and that there was a strong fractionation associated with the dissolution of Fe during initial lava-seawater mixing. In contrast, isotopic signatures similar to basaltic $\delta^{56}Fe$ were measured in tdFe samples at multiple points along the Wailuku River on the Island of Hawai'i (-0.03 ± 0.03‰, 1SD, n = 3) and at 3 coastal sites (-0.10 ± 0.09‰, 1SD) collected prior to our expedition (Table 2C; Fig. 6).

Negative $\delta^{56}Fe$ between −0.2 to −0.8‰ has also been observed in high temperature fluids released from deep ocean hydrothermal vents (Severmann et al., 2004; Rouxel et al., 2008; Bennett et al., 2009). These light values have been ascribed to heavy isotope precipitation in subsurface Fe sulfides or secondary Fe silicates (e.g. Mg-Fe amphibole) at high temperature (Rouxel et al., 2003; Rouxel et al., 2016). Given the short timescales associated with eruption and the low sulfur content of subaerial lava flows (Resing and Sansone, 1999), significant Fe sulfide precipitation appears unlikely. Immediate precipitation of isotopically heavy Fe in high temperature waters surrounding the lava parcel could lead to a release of negative $\delta^{56}Fe$ for the remaining dissolved Fe, but this scenario requires a physical separation between initially precipitated Fe with $\delta^{56}Fe > 0$, and the isotopically light particulate Fe sampled in surface waters during our transect ($\delta^{56}Fe = -0.57 \pm 0.04$‰, 1SD). Release of iron with a negative $\delta^{56}Fe$ signature has also been observed in short term leaching experiments with basalt exposed to hydrochloric acid (Chapman

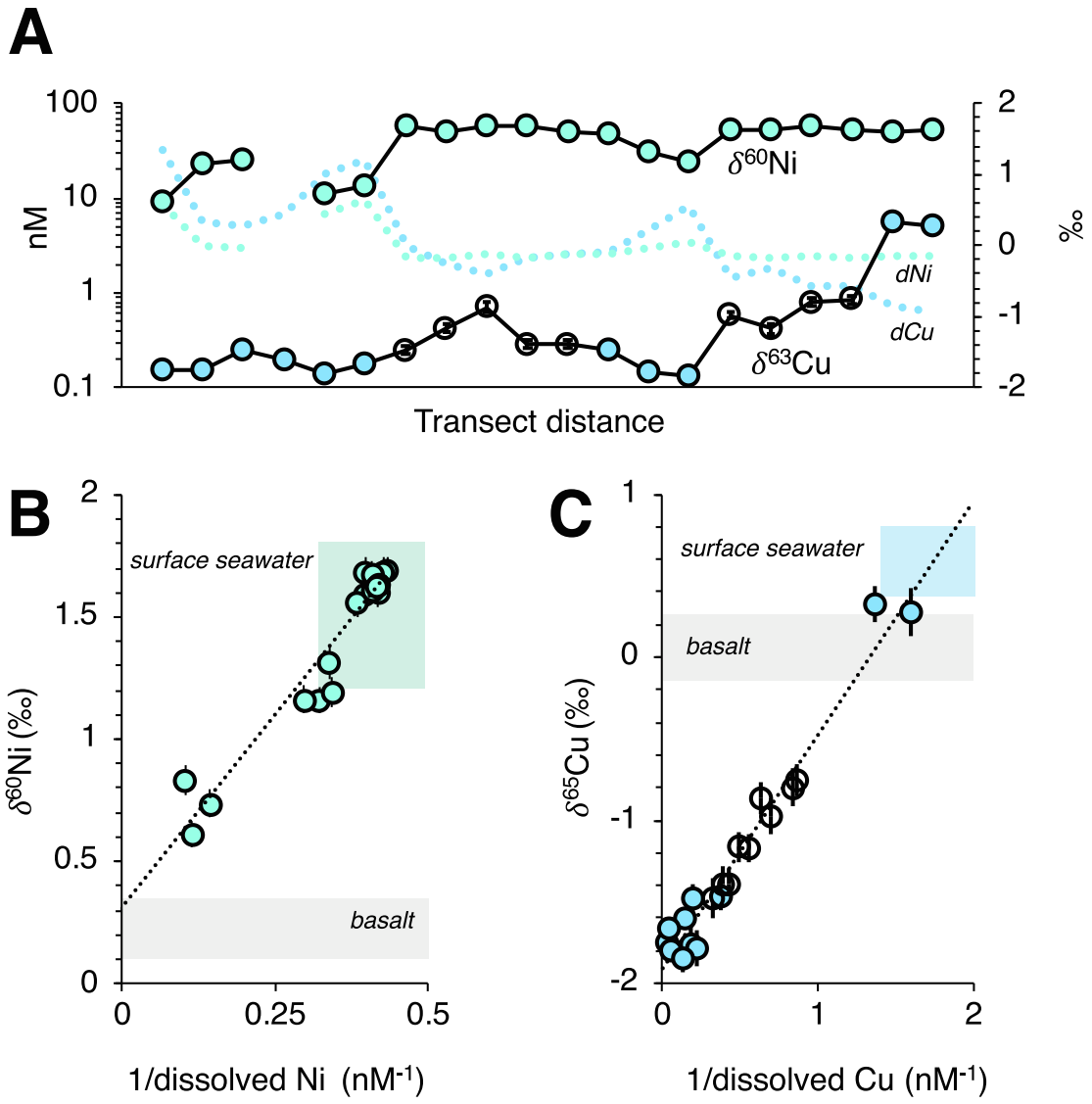

Fig. 7. Nickel and copper isotopic signatures in lava-impacted seawater. (A) Elevated dNi and dCu concentrations (dotted lines, left axis) correspond with decreasing δ^{60}Ni and δ^{65}Cu (green and blue symbols, respectively) across the surface transect. Open circles show Cu samples influenced by dissolution of particles within the cartridge filter (see Discussion). Apparent two component mixing relationships for (B) dNi and δ^{60}Ni ($R^2 = 0.93$) and C) dCu and δ^{65}Cu ($R^2 = 0.96$) between background seawater and the source from lava-seawater interaction. Colored boxes indicate approximate ranges for surface seawater in the Pacific (Cu: Takano et al. (2014); Ni: Takano et al. (2017)). Cu isotope ranges for basalt (grey boxes) are taken from Savage et al., 2015 and Liu et al. (2015), and Ni values are from Gall et al. (2017).

et al., 2009), suggesting that the values reported here can be explained without additional precipitation mechanisms.

Although > 99% of lava-borne iron released to seawater had precipitated by the time it was sampled, dFe concentrations in the plume (5–7 nM) were still an order of magnitude greater than typical dFe values observed in the subtropical North Pacific (<0.5 nM; Brown et al., 2005; Fitzsimmons et al., 2015). The iron isotope composition of dFe collected in waters with high tdFe concentration (>100 nM) was -0.29 ± 0.09 ‰ (1SD, n = 6), which is significantly heavier than the δ^{56}Fe of unfiltered samples (-0.57 ± 0.04 ‰; Fig. 6). In the minor plume sampled further away from the lava entry site, the δ^{56}Fe of dFe increased to $+0.11 \pm 0.06$‰ (1SD, n = 4), even though the δ^{56}Fe of tdFe in this plume was similar to the first (-0.49 ± 0.06‰, 2SE).

Fractionation associated with the redissolution of particulate Fe may be responsible for the increasingly heavy isotopic signatures observed in the dissolved phase. Outside of plume waters, we also note that Fe concentrations in filtered samples often exceeded unfiltered samples by a factor of two (dFe > tdFe; Fig. S5). This suggests that a reservoir of leachable particulate Fe was retained by the cartridge filter while crossing the initial plume and partially dissolved during later sampling. This pattern was also observed for a number of rare earth elements (La, Nd, Ce), which were heavily scavenged in plume waters (Fig. S5). Interestingly the δ^{56}Fe of these 'contaminated' samples was also slightly

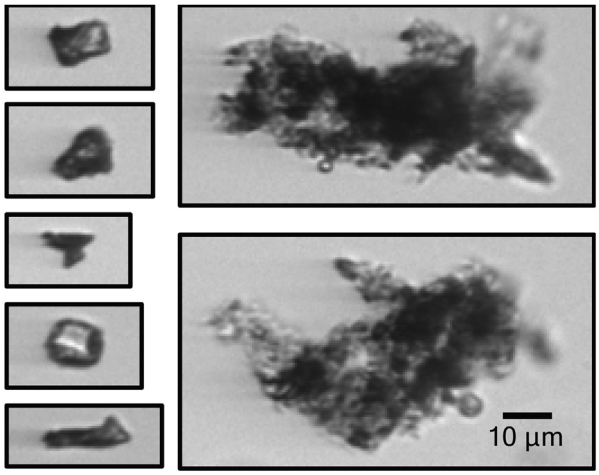

Fig. 8. Micrographs of suspended particles in near-surface waters collected by the Imaging FlowCytoBot (IFCB). Particles were collected within the major plume of lava-impacted seawater where highest particulate Fe (>1 μM) was measured. The images in the left column resemble singular inorganic particles that may be iron oxyhydroxide. The right column shows large aggregates of putative inorganic and organic particles. Note that the brightness of these images has been increased by 50% for visibility.

positive: dFe samples collected between plumes 1 and 2 had a δ^{56}Fe of $+0.12 \pm 0.05$‰ (1 SD) and samples collected after the minor plume had a δ^{56}Fe of $+0.21 \pm 0.07$‰ (1 SD), meaning that both 'contaminated' sets are ~0.7‰ heavier than the δ^{56}Fe of tdFe sampled in the respective plumes (Table 2). Although these data should be interpreted cautiously, it is intriguing that this difference is similar to the δ^{56}Fe offset between soluble Fe in desert dust aerosols (~0.1‰) and the inferred δ^{56}Fe end-member of dust-associated iron supply (+0.68‰) in the North Atlantic Ocean (Conway and John, 2014a). Perhaps this indicates that similar ligand-mediated dissolution mechanisms apply in both scenarios. A transition to heavier dissolved δ^{56}Fe is also observed in the distal South East Pacific Rise plume and associated with ligand dissolution of hydrothermal iron oxyhydroxides (dFe ~ 0.8‰ heavier than leachable particulate Fe; Fitzsimmons et al., 2017).

4.3. Nickel, copper, zinc and cadmium endmembers

The pattern of nickel concentrations was highly similar to Mn, with little evidence for removal of Ni during Fe precipitation (Fig. 4B). Ni isotope measurements showed strong signs of two-endmember mixing, with the highest dNi concentrations (>8 nM) associated with a δ^{60}Ni between +0.6 and +0.8‰ (Fig. 7A). This value is influenced by the heavy isotopic composition of the 2.4 nM dNi in background surface seawater ($+1.63 \pm 0.02$‰, 1 SD, n = 6), which agrees with surface δ^{60}Ni previously reported for the subtropical South Pacific (Takano et al., 2017) and recent measurements in the subtropical North Pacific (Fig. S6; Yang et al., 2020). As a result, the actual source of Ni from lava-seawater interaction is even lighter. Regression between the inverse of dNi and δ^{60}Ni suggests an endmember composition of ~0.3‰ ($R^2 = 0.93$; Fig. 7B). This is very similar to the δ^{60}Ni of the mantle and igneous rocks ($+0.23 \pm 0.07$‰; Gall et al., 2017). Agreement between igneous rock δ^{60}Ni and our inferred endmember implies little fractionation of Ni isotopes during lava dissolution.

In contrast, copper release during mixing of lava and seawater is associated with a very light isotopic composition. In the main plume, dCu reached 25 nM and contained a δ^{65}Cu that ranged between −1.5 and −1.8‰ (Fig. 7A, Table 2). Like Ni, there is a strong relationship between 1/dCu and δ^{65}Cu across our sample set, which strongly suggests two-endmember mixing between a light source of −1.9‰ and background dCu in seawater (+0.5‰ at 0.6 nM, $R^2 = 0.96$; Fig. 7C). This background composition is similar to published measurements of δ^{65}Cu in seawater, which typically ranges between +0.4 to +0.8‰ (Takano et al., 2014; Thompson and Ellwood, 2014; Little et al., 2018), with Cu in the surface ocean being somewhat lighter than deeper waters. The lava source δ^{65}Cu is much lower than the isotopic composition of mid-ocean ridge basalts and ocean island basalts ($+0.06 \pm 0.2$‰; Liu et al., 2015; Savage et al., 2015), or that associated with high temperature hydrothermal fluids (~0‰; Rouxel et al., 2004). Like Fe, it is expected that the lava from the 2018 eruption of Kīlauea contain a δ^{65}Cu that also resembles a value near 0‰, and that fractionation is imposed during high temperature interaction with seawater. Several lines of evidence have suggested that hydrothermal alteration of Cu sulfide minerals is associated with mobilization of heavy δ^{65}Cu (Rouxel et al., 2004; Markl et al., 2006; Seo et al., 2007; Pękala et al., 2011; Sherman, 2013). In this context, the release of isotopically light Cu from lava is unique compared to other hydrothermal processes.

Due to the presence of high concentrations of particulate Fe in plume waters, it may be possible that the anomalous Cu isotopic composition reflects partitioning between dCu and Cu adsorbed onto the surface of Fe oxides. In the main plume, dCu concentrations were ~33% less than tdCu concentrations, suggesting significant scavenging of Cu (Fig. 4C). Therefore, the negative isotope excursions may not reflect the original Cu source but the removal of isotopically heavy Cu onto the surface of Fe oxyhydroxides. However, there are problems with this interpretation. Cu associated with deep ocean ferromanganese crusts is not isotopically heavy relative to seawater δ^{65}Cu (Little et al., 2014b; Little et al., 2014a; Takano et al., 2014). Furthermore, we note that Cu in many filtered samples exceeded Cu in unfiltered samples outside of plume waters, suggesting re-solubilization of scavenged Cu during dissolution of particulate Fe caught in our cartridge filters (Fig. S5). Although unfortunate, contamination in this manner turns out to be quite useful. If the scavenged Cu phase contained a heavy isotopic composition (estimated to be +4‰), its re-dissolution would impart a very heavy δ^{65}Cu fingerprint that is not observed in this sample set. Indeed, linearity between 1/dCu and δ^{65}Cu (Fig. 7C) means that any artifactual re-dissolution of scavenged Cu must occur with a δ^{65}Cu matching the isotopic composition of the original source.

In the main plume, zinc and cadmium were also isotopically light ($\delta^{66}Zn = -0.06 \pm 0.04‰$ and $\delta^{114}Cd = -0.44 \pm 0.24‰$, 1SD, n = 3; Table 2A), relative to basaltic values, $+0.28 \pm 0.05‰$ and $0 \pm 0.1‰$, respectively (Wombacher et al., 2003; Chen et al., 2013). In the case of Cd, the isotopic signature of the lava source may be substantially lower than the measured values in the surface plume. During this expedition, we observed nitrate concentrations on the order of 0.9 μM within the seawater-lava plume. After accounting for fractionation by biological uptake, nitrate in plume waters had an isotopic composition ($\delta^{15}N$ and $\delta^{18}O$) similar to nitrate in subsurface waters found between 300–500 m (Wilson et al., 2019). This suggests a vertical supply of nitrate related to the buoyant heating of mesopelagic waters, which would also bring Cd to the surface. Based on published Cd concentration and isotope profiles in the subtropical North Pacific (Conway and John, 2015), we estimate that ~26% of measured Cd originated from this upwelling mechanism (in addition to dissolution of Cd from lava; Table S2), containing a $\delta^{114}Cd = +0.43 \pm 0.04‰$ (2SE). The presence of isotopically heavy Cd due to upwelling means that the true endmember $\delta^{114}Cd$ associated with lava-seawater interaction is more negative: approximately $-0.73 \pm 0.32‰$. For all other metals, estimated upwelling contributions were negligible (<3%).

There is an unlikely analogy between the magnitude of fractionation of Cu, Cd, and Zn isotopes during lava-seawater interaction (−1.9, −0.7, and −0.3‰, respectively) and the loss of light Cu, Cd, and Zn isotopes in tektites (Fig. 9; Wombacher et al., 2003; Moynier et al., 2009, 2010). Formed during extraterrestrial impact events, tektites are small fragments of Earth's crust that are ejected into the atmosphere at very high temperature, which melt and then cool during flight. Tektites are depleted in Cu relative to parent materials and record a strikingly heavy $\delta^{65}Cu$ signature, up to +12‰ (Rodovská et al., 2017). Loss of light Cu has been attributed to greater diffusion of light Cu isotopes into vapor phases as volatiles are stripped from the melt (Jiang et al., 2019). Volatilization of Zn also leaves behind isotopically heavy signatures in the cooled tektite, but the magnitude of Zn fractionation is not as intense as Cu (Moynier et al., 2009). This is likely related to the greater diffusivity of the Cu^+ ion compared to Zn^{2+}, which enables greater fractionation in the rapidly cooling solid (Ni et al., 2017; Creech et al., 2019). Cd isotopic behavior in tektites has not been systematically investigated, but a single measurement (Wombacher et al., 2003) indicates that loss of light Cd occurs as well. Experimental systems have also indicated large fractionation of light Cd during evaporation (Wombacher et al., 2004).

The chemistry of rapidly cooling lava after contact with seawater may be similar to processes occurring in tektites. Lava is not completely degassed during subaerial flow and previous studies have found enhanced release of volatiles during lava-seawater mixing (Resing and Sansone, 1999), which resembles the 'bubble-stripping' mechanism put forth to explain isotopic patterns in tektites (Jiang et al., 2019). The evolution of volatiles during contact with seawater also seems to result in the preferential release of Cu, Cd, and other elements (e.g. Hg, Pb; Sansone et al., 2002), which may be mobilized by complexation with reduced sulfur species. Indeed, experimental temperature thresholds for Zn and Cu volatilization (1145 °C and 1234 °C, respectively; Sossi et al., 2019) are similar to lava temperatures inferred during the high-volume phase of the 2018 eruption (>1140 °C; Gansecki et al., 2019), suggesting that volatilization is plausible. Despite the higher volatility of Cd and Zn, stronger isotopic fractionation of Cu likely relates to greater diffusivity of monovalent Cu^+ over divalent ions like Zn^{2+} and (presumably) Cd^{2+} (Fig. 10; Ni and Zhang, 2016). In turn, the greater volatility of Cd over Zn may lead to greater isotopic fractionation. The absence of Ni isotope fractionation is also consistent with its much lower volatility. Importantly, there appears

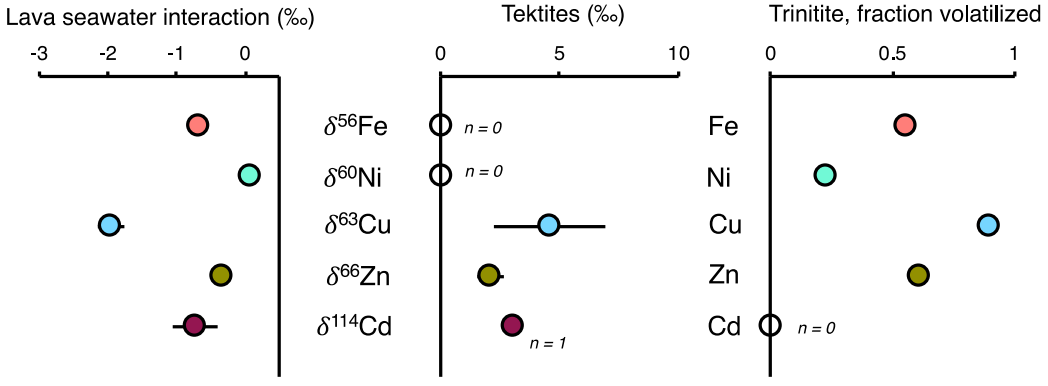

Fig. 9. Comparison of metal isotope fractionation patterns from lava seawater interaction (left) with isotopic signatures observed in tektites (center) and element abundance patterns associated with trinitite (right). Isotopic values for seawater are calculated as the difference between published basalt endmembers and measured values (see main text). Cd isotopic composition is corrected for upwelling of mesopelagic Cd. Heavy isotopic composition of metals in tektites is due to preferential volatilization of light isotopes (see Moynier et al. (2009, 2010), Rodovská et al. (2017) for Cu and Zn data; Wombacher et al. (2003) for Cd data). Elements without data are identified as open circles. The amount of metal volatized near ground zero of the trinity bomb tests (and depletion in the resulting trinitite glass) is taken from Day et al. (2017).

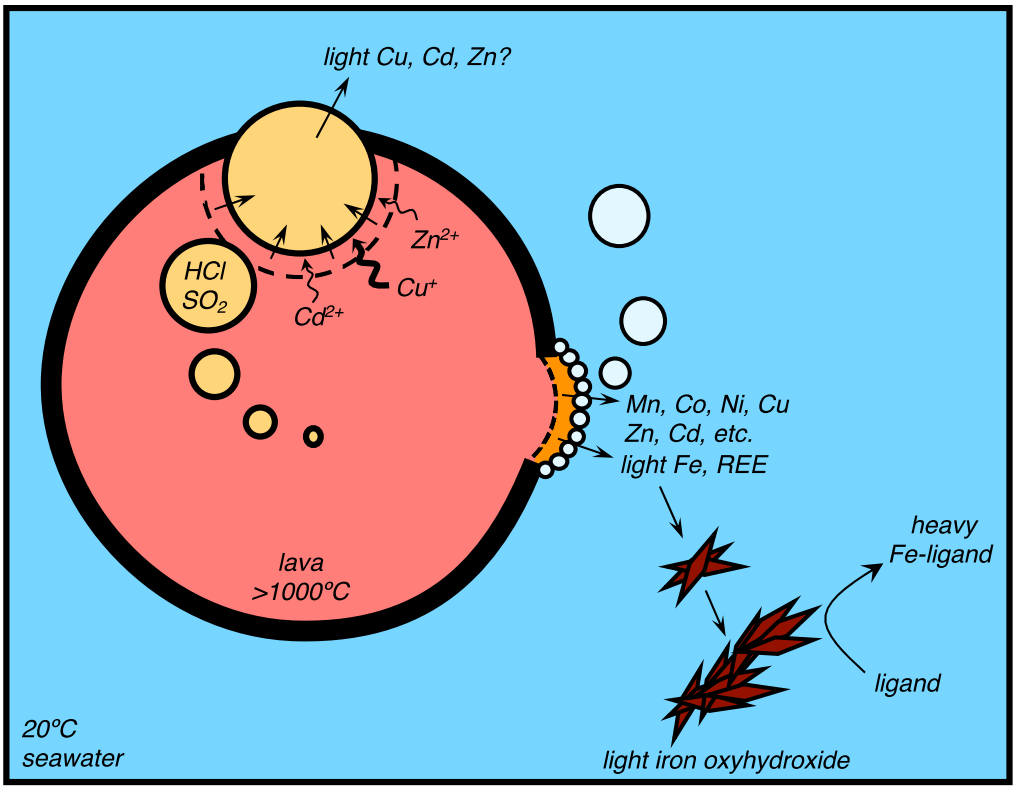

Fig. 10. Mechanisms of metal release during lava-seawater mixture. Congruent dissolution of elements in high temperature lavas is followed by precipitation of iron oxyhydroxides and scavenging of rare earth elements (REE). Partial re-dissolution of precipitated Fe may lead to isotopically heavy dissolved Fe. Volatilization of chalcophile elements in magmatic vapors (yellow) may lead to additional release of Cd, Cu and potentially Zn. The high diffusivity of Cu in particular may compensate for its lower volatility compared to Zn or Cd and impart the strong isotopic fractionation observed in seawater. (For interpretation of the references to colour in this figure legend, the reader is referred to the web version of this article.)

to be no loss of Ni during tektite formation (Goderis et al., 2017). The pattern of isotopic fractionation during lava-seawater mixture also resembles trends in elemental volatilization observed in trinitites – glasses formed during the 1945 Trinity nuclear test – that are depleted in Cu, Zn, and Fe (no Cd data are available; Day et al., 2017). Similar themes of intense temperature gradients, rapid cooling, and volatile outgassing may result in similar behavior of elements in these disparate processes.

4.4. Potential paleo-oceanographic implications

Direct lava-seawater mixing like that observed at Kīlauea is expected to be analogous to processes occurring during the formation of many large igneous provinces, especially oceanic plateaus (see discussion in Resing and Sansone, 1999). Compared to the oceanic cycling of Cu and Ni isotopes, the δ^{60}Ni and δ^{65}Cu signatures associated with lava-seawater interaction are unique and suggest that they might be applied as tracers of lava-seawater interaction associated with past eruptions. The growing dataset of seawater δ^{65}Cu has shown limited variability, mostly between +0.4 and +0.8‰, and sources with isotopic compositions below 0‰ have not yet been identified (Takano et al., 2014; Thompson and Ellwood, 2014; Little et al., 2018; Baconnais et al., 2019). There is also a small range of seawater Ni isotope variability currently reported (+1.2 to +1.8‰), where slightly heavier values in the surface ocean appear to be associated with phytoplankton uptake (Yang et al., 2020; Cameron and Vance, 2014; Takano et al., 2017; Wang et al., 2019; Archer et al., 2020). The general offset between heavy Ni and Cu isotopic composition of rivers and crustal δ^{60}Ni and δ^{65}Cu (0.8‰ and 0.6‰, respectively; Cameron and Vance, 2014; Little et al., 2014b) also implies that typical weathering regimes on land will not produce the +0.3‰ and −1.9‰ signatures observed during the 2018 eruption of Kīlauea.

While the negative values of δ^{114}Cd (as low as −0.7‰) released from lava are also unprecedented in the context of the modern ocean (typically > 0.3‰, Xue et al., 2013; Conway and John, 2015; Yang et al., 2018), there are a number of unrelated processes that strongly affect Cd isotopic composition in the oceans. Both biological uptake by phytoplankton and sulfide precipitation will concentrate light Cd isotopes in particles (Guinoiseau et al., 2018) that will also be buried in marine sediments, obscuring a lava source signature. Similarly, the δ^{66}Zn of lava input (−0.06‰) is typical of Zn isotopic compositions in surface

waters in oligotrophic gyres (Conway and John, 2014b; John et al., 2018). The high variability observed in Fe isotopes at short distances from the site of lava entry also suggests limited utility as a tracer.

Parallel shifts toward lighter δ^{60}Ni and δ^{65}Cu might therefore be the best method to fingerprint direct lava-seawater interaction during past eruptions. Because the δ^{60}Ni signature of lava seawater interaction is crustal and the δ^{65}Cu is significantly lighter, release of these metals by high-temperature lava-seawater interaction can be distinguished from volcanic ash deposition and input by gradual, low temperature weathering of basalt.

However, in order for these signatures to be recorded in sedimentary archives, input must overcome background sources of these elements to the ocean. There is roughly 7×10^8 mol Cu supplied to the oceans from rivers and dust deposition annually, which are much greater than hydrothermal sources (Little et al., 2014b). Assuming a basaltic Cu content of 130 ppm and a density of 3 g cm^{-3}, the 0.8 km^3 of Kīlauea lava erupted during 2018 contained a similar amount of Cu: 5×10^9 mol (Govindaraju, 1994; Neal et al., 2019). Even under ideal conditions (high seawater-lava ratio), the experiments of Resing and Sansone (2002) indicate that 0.03% of Cu in lava is solubilized during contact with seawater (Resing and Sansone, 2002). Therefore, the amount of soluble Cu released from the eruption is probably on the order of 1.5×10^6 mol. A second estimate can be derived from our shipboard observations. Within the major plume, dissolved Cu concentrations exceeded 20 nM over a distance of at least 2 km, with surface currents travelling away from the site of lava entry at 0.5 m s^{-1} (Wilson et al., 2019). If integrated over a 20 m mixed layer and over the 2-month period of eruption (June and July 2018), a similar Cu flux of 2.1×10^6 mol is calculated. While these estimates both represent extrapolations with significant uncertainties, they suggest that the Cu released from the 2018 eruption increased global Cu sources by only 0.1–1%. Given global Ni sources on the order of 3×10^8 moles year^{-1} (Cameron and Vance, 2014), a similar percentage is also predicted for Ni. Thus, eruptions of a similar magnitude are unlikely to alter surface Cu or Ni inventories and may not record isotopic signatures in sedimentary archives.

Although seawater inventories place a relatively high threshold for detection at the basin scale, local/regional scale δ^{65}Cu and δ^{60}Ni signatures may still be preserved in marine sediments, especially during larger eruptions. The massive eruption volumes of several large igneous provinces – amounting to millions of km^3 (Coffin and Eldholm, 1993) – mean that direct effects on ocean ecosystems may have been significant (Wignall, 2001; Tejada et al., 2009). Even with advanced geochronology techniques, however, it can be challenging to decipher if these eruptions took place gradually over hundreds of thousands of years, or as a small number of discrete events (Burgess et al., 2015; Black and Manga, 2017; Schoene et al., 2019). Over a million years, 10^6 km^3 of basalt could be produced from lava supply rates of 1 km^3 year^{-1}, similar to that produced by Kīlauea during 2018 (0.8 km^3). In contrast, century/millennial-length eruptions producing 100–1000 km^3 of lava per year may have occurred. Complications with diagenesis and preservation notwithstanding, detection of parallel Cu and Ni isotopic shifts in marine archives could indicate the magnitude of direct lava-seawater interaction. This would have implications for the rate and mechanism of ocean acidification, deoxygenation, and extinctions that have co-occurred with massive volcanism in the past (Wignall, 2001).

Furthermore, because Cu itself is toxic to many phytoplankton, persistently elevated sources from lava could directly influence the ecosystem responses to massive lava input. We note that the 2018 bloom consisted primarily of *Skeletonema*, a diatom which has an exceptional tolerance to Cu^{2+} ion (Morel et al., 1978; Wilson et al., 2019). In contrast, key diazotrophic species such as *Trichodesmium* – which are highly susceptible to Cu^{2+} toxicity (Rueter et al., 1979) – were not found within the bloom, despite relatively high concentrations of iron and phosphate that ordinarily limit nitrogen fixation in the North Pacific (Ward et al., 2013). If Cu input from lava is sufficient for isotopic shifts in marine sediments to be recorded, it is likely sufficient to cause widespread Cu stress and influence phytoplankton growth.

5. CONCLUSIONS

Perhaps the purest form of hydrothermal interaction, the release of metals during the mixture of molten lava and seawater can be summarized as three distinct processes: (1) a bulk dissolution of elements into seawater in proportion to their abundance in basalt, (2) an additional release of chalcophile elements during degassing of the cooling lava, and (3) precipitation of insoluble elements and subsequent scavenging of 'particle-reactive' elements (Fig. 10). This sequence was described previously by Resing and Sansone (2002) based on seawater and deionized water quenching experiments, but our results from the 2018 eruption demonstrate that these reactions also scale to more intense eruptive events. The elemental abundance patterns in the 2018 seawater plumes – when the flux of lava into the ocean was 50–100 m^3 s^{-1} – was nearly identical to the fingerprint identified in microcosm experiments (Resing and Sansone, 2002). This may indicate that elemental release is primarily controlled by fine scale surface processes, such as the cracking of cooled lava and exposure of new high-temperature interfaces. Indeed, we have estimated a similar magnitude of Cu flux ($1.5–2.1 \times 10^6$ mol) based on independent estimates derived from our oceanographic observations during the 2018 eruption and the extrapolations of prior microcosm results.

The impact of these three primary reactions is also evident in the unusual isotopic composition of several metals in the lava-impacted seawater. The simplest case is for dissolved Ni, which reflects dissolution of basaltic δ^{60}Ni and dilution with seawater δ^{60}Ni. In contrast, lighter Cu, Zn, and Cd isotopic compositions, relative to basalt, points to independent input processes, likely related to volatilization reactions within the rapidly cooling lava. It is unclear if similar reactions also contribute to the release of negative δ^{56}Fe, which has also been observed in other hydrothermal

systems (Severmann et al., 2004). Regardless, the trend towards heavier dissolved δ^{56}Fe with distance away from the lava entry site indicates that the δ^{56}Fe signature is defined less by the endmember value than by isotope fractionation effects during solubilization of particulate Fe, which may also apply to other important iron sources to the ocean, such as deep ocean hydrothermal vents or dissolution of dust-borne Fe. Similar isotopic signatures – especially Cu – released from large eruptions on ocean islands, island arcs, mid ocean ridges, and large igneous provinces may be embedded in marine sediment and sedimentary rock archives, waiting to be discovered.

Declaration of Competing Interest

The authors declare that they have no known competing financial interests or personal relationships that could have appeared to influence the work reported in this paper.

ACKNOWLEDGEMENTS

We thank the Captain and Crew of the R/V Ka'imikai-O-Kanaloa, the Ocean Technology Group (OTG) and all participants of the HOT-LAVA expedition, especially Blake Watkins for assistance with tow-fish deployment. The expedition and analyses were supported by the Simons Foundation Grant 329108 to SGJ, DMK and AEW, NSF RAPID grant OCE-1842012 to DMK, and a Simons Foundation Marine Microbial Ecology and Evolution postdoctoral fellowship to NJH (602538). We acknowledge the use of imagery and satellite data from the NASA Worldview application (https://worldview.earthdata.nasa.gov), part of the NASA Earth Observing System Data and Information System (EOSDIS). The authors thank Angela Knapp and collaborators in the SCOPE program for helpful discussions, as well as Mark Rehkämper, Joseph Resing and 2 anonymous reviewers for comments that significantly improved the manuscript.

APPENDIX A. SUPPLEMENTARY MATERIAL

Supplementary data to this article can be found online at https://doi.org/10.1016/j.gca.2020.05.005.

REFERENCES

Abouchami W., Galer S. J. G., Horner T. J., Rehkämper M., Wombacher F., Xue Z., Lambelet M., Gault-Ringold M., Stirling C. H. and Schönbächler M. (2013) A common reference material for cadmium isotope studies–NIST SRM 3108. *Geostand. Geoanalytical Res.* **37**, 5–17.

Archer C., Andersen M. B., Cloquet C., Conway T. M., Dong S., Ellwood M., Moore R., Nelson J., Rehkämper M. and Rouxel O. (2017) Inter-calibration of a proposed new primary reference standard AA-ETH Zn for zinc isotopic analysis. *J. Anal. At. Spectrom.* **32**, 415–419.

Archer C., Vance D., Milne A. and Lohan M. C. (2020) The oceanic biogeochemistry of nickel and its isotopes: New data from the South Atlantic and the Southern Ocean biogeochemical divide. *Earth Planet. Sci. Lett.* **535** 116118.

Baconnais I., Rouxel O., Dulaquais G. and Boye M. (2019) Determination of the copper isotope composition of seawater revisited: A case study from the Mediterranean Sea. *Chem. Geol.* **511**, 465–480.

Bennett S. A., Rouxel O., Schmidt K., Garbe-Schönberg D., Statham P. J. and German C. R. (2009) Iron isotope fractionation in a buoyant hydrothermal plume, 5 S Mid-Atlantic Ridge. *Geochim. Cosmochim. Acta* **73**, 5619–5634.

Biller D. V. and Bruland K. W. (2012) Analysis of Mn, Fe Co, Ni, Cu, Zn, Cd, and Pb in seawater using the Nobias-chelate PA1 resin and magnetic sector inductively coupled plasma mass spectrometry (ICP-MS). *Mar. Chem.* **130–131**, 12–20.

Black B. A. and Manga M. (2017) Volatiles and the tempo of flood basalt magmatism. *Earth Planet. Sci. Lett.* **458**, 130–140.

Brown M. T., Landing W. M. and Measures C. I. (2005) Dissolved and particulate Fe in the western and central North Pacific: Results from the 2002 IOC cruise. *Geochem., Geophys. Geosyst.* **6**.

Bruland K. W. (1980) Oceanographic distributions of cadmium, zinc, nickel, and copper in the North Pacific. *Earth Planet. Sci. Lett.* **47**, 176–198.

Bryan S. E., Peate I. U., Peate D. W., Self S., Jerram D. A., Mawby M. R., Marsh J. S. G. and Miller J. A. (2010) The largest volcanic eruptions on Earth. *Earth-Sci. Rev.* **102**, 207–229.

Burgess S. D., Bowring S. A., Fleming T. H. and Elliot D. H. (2015) High-precision geochronology links the Ferrar large igneous province with early-Jurassic ocean anoxia and biotic crisis. *Earth Planet. Sci. Lett.* **415**, 90–99.

Cameron V. and Vance D. (2014) Heavy nickel isotope compositions in rivers and the oceans. *Geochim. Cosmochim. Acta* **128**, 195–211.

Chapman J. B., Weiss D. J., Shan Y. and Lemburger M. (2009) Iron isotope fractionation during leaching of granite and basalt by hydrochloric and oxalic acids. *Geochim. Cosmochim. Acta* **73**, 1312–1324.

Chen H., Savage P. S., Teng F.-Z., Helz R. T. and Moynier F. (2013) Zinc isotope fractionation during magmatic differentiation and the isotopic composition of the bulk Earth. *Earth Planet. Sci. Lett.* **369**, 34–42.

Coffin M. F. and Eldholm O. (1993) Scratching the surface: Estimating dimensions of large igneous provinces. *Geology* **21**, 515–518.

Conway T. M. and John S. G. (2014a) Quantification of dissolved iron sources to the North Atlantic Ocean. *Nature* **511**, 212.

Conway T. M. and John S. G. (2014b) The biogeochemical cycling of zinc and zinc isotopes in the North Atlantic Ocean. *Global Biogeochem. Cycles* **28**, 1111–1128.

Conway T. M. and John S. G. (2015) The cycling of iron, zinc and cadmium in the North East Pacific Ocean-Insights from stable isotopes. *Geochim. Cosmochim. Acta* **164**, 262–283.

Conway T. M., Rosenberg A. D., Adkins J. F. and John S. G. (2013) A new method for precise determination of iron, zinc and cadmium stable isotope ratios in seawater by double-spike mass spectrometry. *Anal. Chim. Acta* **793**, 44–52.

Cowen J. P., Massoth G. J. and Feely R. A. (1990) Scavenging rates of dissolved manganese in a hydrothermal vent plume. *Deep Sea Res. Part A. Oceanogr. Res. Pap.* **37**, 1619–1637.

Creech J. B., Moynier F. and Koeberl C. (2019) Volatile loss under a diffusion-limited regime in tektites: Evidence from tin stable isotopes. *Chem. Geol.*, 119279.

Day J. M. D., Moynier F., Meshik A. P., Pradivtseva O. V. and Petit D. R. (2017) Evaporative fractionation of zinc during the first nuclear detonation. *Sci. Adv.* **3**, e1602668.

Fitzsimmons J. N., Hayes C. T., Al-Subiai S. N., Zhang R., Morton P. L., Weisend R. E., Ascani F. and Boyle E. A. (2015) Daily to decadal variability of size-fractionated iron and iron-binding ligands at the Hawaii Ocean Time-series Station ALOHA. *Geochim. Cosmochim. Acta* **171**, 303–324.

Fitzsimmons J. N., John S. G., Marsay C. M., Hoffman C. L., Nicholas S. L., Toner B. M., German C. R. and Sherrell R. M.

(2017) Iron persistence in a distal hydrothermal plume supported by dissolved–particulate exchange. *Nat. Geosci.* **10**, 195.
Fröllje H., Pahnke K., Schnetger B., Brumsack H.-J., Dulai H. and Fitzsimmons J. N. (2016) Hawaiian imprint on dissolved Nd and Ra isotopes and rare earth elements in the central North Pacific: local survey and seasonal variability. *Geochim. Cosmochim. Acta* **189**, 110–131.
Gall L., Williams H. M., Halliday A. N. and Kerr A. C. (2017) Nickel isotopic composition of the mantle. *Geochim. Cosmochim. Acta* **199**, 196–209.
Gansecki C., Lee R. L., Shea T., Lundblad S. P., Hon K. and Parcheta C. (2019) The tangled tale of Kīlauea's 2018 eruption as told by geochemical monitoring. *Science (80-.)* **366**, eaaz0147. Available at: http://science.sciencemag.org/content/366/6470/eaaz0147.abstract.
Goderis S., Tagle R., Fritz J., Bartoschewitz R. and Artemieva N. (2017) On the nature of the Ni-rich component in splash-form Australasian tektites. *Geochim. Cosmochim. Acta* **217**, 28–50.
Govindaraju K. (1994) 1994 compilation of working values and sample description for 383 geostandards. *Geostand. Newsl.* **18**, 1–158.
Guinoiseau D., Galer S. J. G. and Abouchami W. (2018) Effect of cadmium sulphide precipitation on the partitioning of Cd isotopes: Implications for the oceanic Cd cycle. *Earth Planet. Sci. Lett.* **498**, 300–308.
Hawco N. J., Lam P. J., Lee J., Ohnemus D. C., Noble A. E., Wyatt N. J., Lohan M. C. and Saito M. A. (2018) Cobalt scavenging in the mesopelagic ocean and its influence on global mass balance : Synthesizing water column and sedimentary fluxes. *Mar. Chem.* **201**, 151–166.
Jiang Y., Chen H., Fegley, Jr, B., Lodders K., Hsu W., Jacobsen S. B. and Wang K. (2019) Implications of K, Cu and Zn isotopes for the formation of tektites. *Geochim. Cosmochim. Acta* **259**, 170–187.
John S. G., Helgoe J. and Townsend E. (2018) Biogeochemical cycling of Zn and Cd and their stable isotopes in the Eastern Tropical South Pacific. *Mar. Chem.* **201**, 256–262.
Klinkhammer G., Bender M. and Weiss R. F. (1977) Hydrothermal manganese in the Galapagos Rift. *Nature* **269**, 319.
Klinkhammer G., Rona P., Greaves M. and Elderfield H. (1985) Hydrothermal manganese plumes in the Mid-Atlantic Ridge rift valley. *Nature* **314**, 727.
Little S. H., Archer C., Milne A., Schlosser C., Achterberg E. P., Lohan M. C. and Vance D. (2018) Paired dissolved and particulate phase Cu isotope distributions in the South Atlantic. *Chem. Geol.* **502**, 29–43.
Little S. H., Sherman D. M., Vance D. and Hein J. R. (2014a) Molecular controls on Cu and Zn isotopic fractionation in Fe–Mn crusts. *Earth Planet. Sci. Lett.* **396**, 213–222.
Little S. H., Vance D., Walker-Brown C. and Landing W. M. (2014b) The oceanic mass balance of copper and zinc isotopes, investigated by analysis of their inputs, and outputs to ferromanganese oxide sediments. *Geochim. Cosmochim. Acta* **125**, 673–693.
Liu S.-A., Huang J., Liu J., Wörner G., Yang W., Tang Y.-J., Chen Y., Tang L., Zheng J. and Li S. (2015) Copper isotopic composition of the silicate Earth. *Earth Planet. Sci. Lett.* **427**, 95–103.
Markl G., Lahaye Y. and Schwinn G. (2006) Copper isotopes as monitors of redox processes in hydrothermal mineralization. *Geochim. Cosmochim. Acta* **70**, 4215–4228.
Milne A., Landing W., Bizimis M. and Morton P. (2010) Determination of Mn, Fe Co, Ni, Cu, Zn, Cd and Pb in seawater using high resolution magnetic sector inductively coupled mass spectrometry (HR-ICP-MS). *Anal. Chim. Acta* **665**, 200–207.
Moffett J. W. and Ho J. (1996) Oxidation of cobalt and manganese in seawater via a common microbially catalyzed pathway. *Geochim. Cosmochim. Acta* **60**, 3415–3424.
Morel N. M. L., Rueter J. C. and Morel F. M. M. (1978) Copper toxicity to Skeletonema costatum (Bacillariophyceae). *J. Phycol.* **14**, 43–48.
Moynier F., Beck P., Jourdan F., Yin Q.-Z., Reimold U. and Koeberl C. (2009) Isotopic fractionation of zinc in tektites. *Earth Planet. Sci. Lett.* **277**, 482–489.
Moynier F., Koeberl C., Beck P., Jourdan F. and Telouk P. (2010) Isotopic fractionation of Cu in tektites. *Geochim. Cosmochim. Acta* **74**, 799–807.
Neal C. A., Brantley S. R., Antolik L., Babb J. L., Burgess M., Calles K., Cappos M., Chang J. C., Conway S. and Desmither L. (2019) The 2018 rift eruption and summit collapse of Kīlauea Volcano. Science (80-.). 363, 367–374.
Ni P. and Zhang Y. (2016) Cu diffusion in a basaltic melt. *Am. Mineral.* **101**, 1474–1482.
Ni P., Zhang Y., Simon A. and Gagnon J. (2017) Cu and Fe diffusion in rhyolitic melts during chalcocite "dissolution": Implications for porphyry ore deposits and tektites. *Am. Mineral. J. Earth Planet. Mater.* **102**, 1287–1301.
Pękala M., Asael D., Butler I. B., Matthews A. and Rickard D. (2011) Experimental study of Cu isotope fractionation during the reaction of aqueous Cu (II) with Fe (II) sulphides at temperatures between 40 and 200 C. *Chem. Geol.* **289**, 31–38.
Posacka A. M., Semeniuk D. M., Whitby H., van den Berg C. M. G., Cullen J. T., Orians K. and Maldonado M. T. (2017) Dissolved copper (dCu) biogeochemical cycling in the subarctic Northeast Pacific and a call for improving methodologies. *Mar. Chem.* **196**, 47–61.
Resing J. A. and Sansone F. J. (2002) The chemistry of lava-seawater interactions II: The elemental signature. *Geochim. Cosmochim. Acta* **66**, 1925–1941.
Resing J. A. and Sansone F. J. (1999) The chemistry of lava–seawater interactions: The generation of acidity. *Geochim. Cosmochim. Acta* **63**, 2183–2198.
Resing J. A., Sedwick P. N., German C. R., Jenkins W. J., Moffett J. W., Sohst B. M. and Tagliabue A. (2015) Basin-scale transport of hydrothermal dissolved metals across the South Pacific Ocean. *Nature* **523**, 200.
Rodovská Z., Magna T., Žák K., Kato C., Savage P. S., Moynier F., Skála R. and Ježek J. (2017) Implications for behavior of volatile elements during impacts—Zinc and copper systematics in sediments from the Ries impact structure and central European tektites. *Meteorit. Planet. Sci.* **52**, 2178–2192.
Rouxel O., Dobbek N., Ludden J. and Fouquet Y. (2003) Iron isotope fractionation during oceanic crust alteration. *Chem. Geol.* **202**, 155–182.
Rouxel O., Fouquet Y. and Ludden J. N. (2004) Copper isotope systematics of the Lucky Strike, Rainbow, and Logatchev sea-floor hydrothermal fields on the Mid-Atlantic Ridge. *Econ. Geol.* **99**, 585–600.
Rouxel O., Shanks, III, W. C., Bach W. and Edwards K. J. (2008) Integrated Fe-and S-isotope study of seafloor hydrothermal vents at East Pacific Rise 9–10 N. *Chem. Geol.* **252**, 214–227.
Rouxel O., Toner B. M., Manganini S. J. and German C. R. (2016) Geochemistry and iron isotope systematics of hydrothermal plume fall-out at East Pacific Rise 9 50′ N. *Chem. Geol.* **441**, 212–234.
Rubin K. (1997) Degassing of metals and metalloids from erupting seamount and mid-ocean ridge volcanoes: Observations and predictions. *Geochim. Cosmochim. Acta* **61**, 3525–3542.
Rueter J. G., McCarthy J. J. and Carpenter E. J. (1979) The toxic effect of copper on Oscillatoria (Trichodesmium) theibautii 1. *Limnol. Oceanogr.* **24**, 558–562.

Sansone F. J., Benitez-Nelson C. R., Resing J. A., DeCarlo E. H., Vink S. M., Heath J. A. and Huebert B. J. (2002) Geochemistry of atmospheric aerosols generated from lava-seawater interactions. *Geophys. Res. Lett.* **29**, 41–49.

Savage P. S., Moynier F., Chen H., Shofner G., Siebert J., Badro J. and Puchtel I. S. (2015) Copper isotope evidence for large-scale sulphide fractionation during Earth's differentiation. *Geochem. Perspect. Lett.*.

Schoene B., Eddy M. P., Samperton K. M., Keller C. B., Keller G., Adatte T. and Khadri S. F. R. (2019) U-Pb constraints on pulsed eruption of the Deccan Traps across the end-Cretaceous mass extinction. *Science* **80**, 363, 862–866.

Sedwick P. N., McMurtry G. M. and Tribble G. W. (1991) Chemical alteration of seawater by lava from Kilauea Volcano, Hawaii. *Mar. Geol.* **96**, 151–158.

Seo J. H., Lee S. K. and Lee I. (2007) Quantum chemical calculations of equilibrium copper (I) isotope fractionations in ore-forming fluids. *Chem. Geol.* **243**, 225–237.

Severmann S., Johnson C. M., Beard B. L., German C. R., Edmonds H. N., Chiba H. and Green D. R. H. (2004) The effect of plume processes on the Fe isotope composition of hydrothermally derived Fe in the deep ocean as inferred from the Rainbow vent site, Mid-Atlantic Ridge, 36 14′ N. *Earth Planet. Sci. Lett.* **225**, 63–76.

Sherman D. M. (2013) Equilibrium isotopic fractionation of copper during oxidation/reduction, aqueous complexation and ore-forming processes: Predictions from hybrid density functional theory. *Geochim. Cosmochim. Acta* **118**, 85–97.

Sossi P. A., Klemme S., O'Neill H. S. C., Berndt J. and Moynier F. (2019) Evaporation of moderately volatile elements from silicate melts: experiments and theory. *Geochim. Cosmochim. Acta* **260**, 204–231.

Stevenson E. I., Fantle M. S., Das S. B., Williams H. M. and Aciego S. M. (2017) The iron isotopic composition of subglacial streams draining the Greenland ice sheet. *Geochim. Cosmochim. Acta* **213**, 237–254.

Sunda W. G. and Huntsman S. A. (1988) Effect of sunlight on redox cycles of manganese in the southwestern Sargasso Sea. *Deep Sea Res. Part A. Oceanogr. Res. Pap.* **35**, 1297–1317.

Takano S., Tanimizu M., Hirata T., Shin K.-C., Fukami Y., Suzuki K. and Sohrin Y. (2017) A simple and rapid method for isotopic analysis of nickel, copper, and zinc in seawater using chelating extraction and anion exchange. *Anal. Chim. Acta* **967**, 1–11.

Takano S., Tanimizu M., Hirata T. and Sohrin Y. (2014) Isotopic constraints on biogeochemical cycling of copper in the ocean. *Nat. Commun.* **5**, 5663.

Tejada M. L. G., Suzuki K., Kuroda J., Coccioni R., Mahoney J. J., Ohkouchi N., Sakamoto T. and Tatsumi Y. (2009) Ontong Java Plateau eruption as a trigger for the early Aptian oceanic anoxic event. *Geology* **37**, 855–858.

Teng F.-Z., Dauphas N. and Helz R. T. (2008) Iron isotope fractionation during magmatic differentiation in Kilauea Iki lava lake. *Science (80-.)* **320**, 1620–1622.

Teng F.-Z., Dauphas N., Huang S. and Marty B. (2013) Iron isotopic systematics of oceanic basalts. *Geochim. Cosmochim. Acta* **107**, 12–26.

Thompson C. M. and Ellwood M. J. (2014) Dissolved copper isotope biogeochemistry in the Tasman Sea, SW Pacific Ocean. *Mar. Chem.* **165**, 1–9.

Wang R.-M., Archer C., Bowie A. R. and Vance D. (2019) Zinc and nickel isotopes in seawater from the Indian Sector of the Southern Ocean: The impact of natural iron fertilization versus Southern Ocean hydrography and biogeochemistry. *Chem. Geol.* **511**, 452–464.

Ward B. A., Dutkiewicz S., Moore C. M. and Follows M. J. (2013) Iron, phosphorus, and nitrogen supply ratios define the biogeography of nitrogen fixation. *Limnol. Oceanogr.* **58**, 2059–2075.

Wignall P. B. (2001) Large igneous provinces and mass extinctions. *Earth-Sci. Rev.* **53**, 1–33.

Wilson Samuel T., Hawco Nicholas J., Armbrust E. Virgini, Barone Benedett, Björkman Karin M., Boysen Angela K., Burgos Macaren, Burrell Timothy J., Casey John R., DeLong Edward F., Dugenne Mathild, Dutkiewicz Stephani, Dyhrman Sonya T., Ferrón Sar, Follows Michael J., Foreman Rhea K., Funkey Carolina P., Harke Matthew J., Henke Britt A., Hill Christopher N., Hynes Annette M., Ingalls Anitra E., Jahn Olive, Kelly Rachel L., Knapp Angela N., Letelier Ricardo M., Ribalet Francoi, Shimabukuro Eric M., Tabata Ryan K. S., Turk-Kubo Kendra A., White Angelicque E., Zehr Jonathan P., John Set and Karl David M. (2019) Kīlauea lava fuels phytoplankton bloom in the North Pacific Ocean. *Science* **365** (6457), 1040–1044. https://doi.org/10.1126/science:aax4767.

Wombacher F., Rehkämper M. and Mezger K. (2004) Determination of the mass-dependence of cadmium isotope fractionation during evaporation. *Geochim. Cosmochim. Acta* **68**, 2349–2357.

Wombacher F., Rehkämper M., Mezger K. and Münker C. (2003) Stable isotope compositions of cadmium in geological materials and meteorites determined by multiple-collector ICPMS. *Geochim. Cosmochim. Acta* **67**, 4639–4654.

Xue Z., Rehkämper M., Horner T. J., Abouchami W., Middag R., van de Flierd T. and de Baar H. J. W. (2013) Cadmium isotope variations in the Southern Ocean. *Earth Planet. Sci. Lett.* **382**, 161–172.

Yang S.-C., Zhang J., Sohrin Y. and Ho T.-Y. (2018) Cadmium cycling in the water column of the Kuroshio-Oyashio Extension region: Insights from dissolved and particulate isotopic composition. *Geochim. Cosmochim. Acta* **233**, 66–80.

Yang S.-C., Hawco N. J., Pinedo-Gonzalez P., Bian X., Huang K.-F., Zhang R. and John S. G. (2020) A new purification method for Ni and Cu stable isotopes in seawater provides evidence for widespread Ni isotope fractionation by phytoplankton in the North Pacific. *Chem. Geol.* **547,** 119662.

Associate editor: Mark Rehkamper